Article

# Theoretical and Experimental Investigation of the Tb³⁺ → Eu³⁺ Energy Transfer Mechanisms in Cubic A₃Tb₀.₉₀Eu₀.₁₀(PO₄)₃ (A = Sr, Ba) Materials

Albano N. Carneiro Neto, Renaldo T. Moura Jr., Andrii Shyichuk, Veronica Paterlini, Fabio Piccinelli, Marco Bettinelli,* and Oscar L. Malta*

Read Online

ACCESS | Metrics & More | Article Recommendations | SI Supporting Information

**ABSTRACT:** In this study the optical spectroscopy, the excited state dynamics, and in particular the Tb³⁺ → Eu³⁺ energy transfer, have been investigated in detail both from the theoretical and experimental point of view in eulytite double phosphate hosts A₃Tb(PO₄)₃ (A = Sr, Ba) doped with Eu³⁺. It has been found that the energy transfer is strongly assisted by fast migration in the donor Tb³⁺ subset. Moreover, the transfer rates and efficiencies depend significantly on the nature of the divalent elements present in the structure and hence on the distances between Tb³⁺-Eu³⁺ nearest neighbors. It is shown that the competition between quadrupole−quadrupole and exchange interaction is crucial in accounting for the transfer rates.
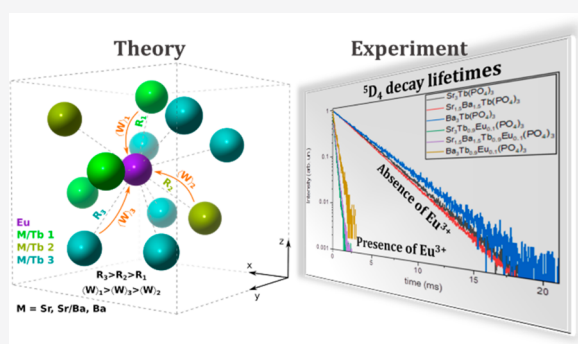
## 1. INTRODUCTION

An important goal in the development of luminescent material is the possibility of fine-tuning their optical properties, in order to obtain the desired features of the emitted light. This is usually possible thanks to a detailed knowledge of structure−property relationships. One of the most interesting and promising phenomena occurring in luminescent materials is energy transfer (ET),[1] allowing a wide range of applications in the fields of biosensing, phosphors, scintillators design, and nanothermometry.[2−6] ET consists in the nonradiative transfer of energy from a donor (D) excited species to an unexcited acceptor (A), with the first species relaxing to a lower state and the latter being excited[7,8] and can occur through several mechanisms: electric multipole-multipole, magnetic dipole−dipole, and exchange.[9]

When ET occurs in inorganic materials containing lanthanide ions (Ln³⁺), the luminescence is strongly dependent on the efficiency and rate of this process. In view of the possible applications, the knowledge of the precise mechanisms is undoubtedly important,[10] since each of them depends in a different way on several parameters and can give rise to a wide range of transfer rates. However, a deep understanding of the mechanisms governing the ET is often difficult, since the literature is rich in misconceptions.[7,11] This is partly due to the different formulations required for Ln³⁺ ions with respect to organic molecules and to the continuously evolving studies about the optimization of the parameters that influence the ET rates.

All the aforementioned mechanisms are strongly distance dependent between the centers involved in the transfer process ($R_L$). In particular, the ET rates for electric dipole-electric dipole ($W_{d−d}$), electric dipole-electric quadrupole ($W_{d−q}$), and electric quadrupole-electric quadrupole ($W_{q−q}$) mechanisms are dependent on $R_L^{-6}$, $R_L^{-8}$, $R_L^{-10}$, respectively;[9,12] the exchange transfer rate ($W_{ex}$) decreases exponentially with increasing $R_L$,[9] and finally, the magnetic dipole-magnetic dipole ($W_{md−md}$) transfer rate shows the same distance dependence as $W_{d−d}$.[10,12,13] In the case of transfer between Ln³⁺ ions, the exchange mechanism becomes significant for separations between D and A lower than 4 Å.[7,10,12,14] This interaction makes transfer to A occur also when the electric multipolar interactions are forbidden.[9]

In the literature about Ln³⁺ ions, due to the influence of the previous research concerning organic molecules, it has often been taken for granted that the $W_{d−d}$ interactions are systematically prevalent on the other types of mechanism. However, after the inclusions of appropriate shielding effects for 4f levels, due to 5s and 5p subshell in the Coulomb contribution,[10] and by improving the necessary thermal models, it has recently been shown that $W_{q−q}$ is the dominant
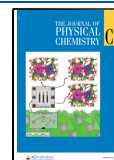
interaction governing energy transfer in elpasolite cubic materials.[11]

Host sensitization takes place when the D concentration is large, and D is part of the bulk material instead of an impurity.[9,12] In this case, also nonradiative transfer between two identical D centers can occur, from one excited D species to another one, in the ground state. This resonant transfer process is called migration and proceeds until the energy is transferred to a nonemitting trap or to a different emitting species.[7,12]

Particularly, in materials containing $Tb^{3+}$ ions as a component of the host and $Eu^{3+}$ ions as a doping element, ET from $Tb^{3+}$ to $Eu^{3+}$ has been widely investigated.[3,15−18] Both exchange interaction and migration were found to contribute to the $Tb^{3+} \rightarrow Eu^{3+}$ ET.[18,19]

In the present work, the relationship between ET efficiency and the ions distance has been carefully investigated. Experimental results have been compared with theoretical analysis in order to determine the dominant physical mechanisms governing $Tb^{3+} \rightarrow Eu^{3+}$ ET. With this aim in mind, a relatively simple system has been considered: cubic eulytite structures with the general formula $A_3Tb_{0.90}Eu_{0.10}(PO_4)_3$, where A is a divalent cation. Here, $Tb^{3+}$ is an ion constituting the host compound, while $Eu^{3+}$ is present as a dopant. The same structure was maintained when the A atom is either $Sr^{2+}$ or $Ba^{2+}$, or a mixture of 50% $Sr^{2+}$ and 50% $Ba^{2+}$, with a resulting change in cell parameters and consequently $Tb^{3+}–Tb^{3+}$ and $Tb^{3+}–Eu^{3+}$ separation. This has allowed a detailed study of the distance dependence of the ET process.

A reformulation based on Kushida's[13] and Dexter's[9] equations for the multipolar and exchange mechanisms of ET rates will be tested. This reformulation, as treated in references,[10,11,20] emphasizes the importance of shielding effects and the use of the forced electric dipole intensity parameters (Judd-Ofelt theory) instead of the use of experimental values which include the dynamic coupling mechanism.[8]

## 2. EXPERIMENTAL SECTION

Eulytites double phosphates were synthesized by solid state reaction, through two heat treatments at 1250 °C for 48 h (as described by Barbier et al.[21]). A rapid quenching to room temperature was necessary in order to avoid the formation of simple phosphates.

XRD analysis were performed by means of a Thermo ARL X'TRA powder diffractometer instrument, equipped with a Cu-anode as an X-ray source and a cooled solid state detector Peltier Si(Li). Bragg−Brentano geometry was used, and the measurement setup was a 1.2°/min scan rate, a 1.5 s integration time, and a 5−90° 2θ range.

The Fluorolog 3 spectrofluorometer (Horiba-Jobin Yvon) was used to collect both luminescence spectra and lifetimes, with a Xe lamp as the excitation source, a double excitation monochromator, a single emission monochromator, and a PMT detector. Decays curves were measured in the TCSPC mode with a Xe microsecond pulsed lamp.

## 3. THEORETICAL

### 3.1. Theoretical Intensity Parameters.
The forced electric dipole (FED; Judd-Ofelt theory) and dynamic coupling (DC) mechanisms are the most responsible for the 4f−4f intensities when the lanthanide occupy a noncentrosymmetric site.[22−24] The theoretical expressions here used for the intensity parameters, $\Omega_\lambda^{\text{theo}}$, have been described in detail in several references.[25−29] However, it might be worth briefly recalling them:

$$\Omega_\lambda^{\text{theo}} = (2\lambda + 1) \sum_{t,p} \frac{|B_{\lambda tp}|^2}{2t + 1}, \quad B_{\lambda tp} = B_{\lambda tp}^{\text{FED}} + B_{\lambda tp}^{\text{DC}} \tag{1}$$

where

$$B_{\lambda tp}^{\text{FED}} = \frac{2}{\Delta E}\langle r^{t+1}\rangle\Theta(t,\lambda)\left(\frac{4\pi}{2t+1}\right)^{1/2}\sum_j \frac{e^2\rho_j g_j(2\beta_j)^{t+1}}{R_j^{t+1}}(Y_p^{t*})_j \tag{2}$$

$$B_{\lambda tp}^{\text{DC}} = -\left[\frac{(\lambda+1)(2\lambda+3)}{(2\lambda+1)}\right]^{1/2}\langle r^\lambda\rangle\langle f\|C^{(\lambda)}\|f\rangle\left(\frac{4\pi}{2t+1}\right)^{1/2}$$
$$\times \sum_j \frac{[(2\beta_j)^{t+1}\alpha_{OP,j} + \alpha_j']}{R_j^{t+1}}(Y_p^{t*})_j\delta_{t,\lambda+1} \tag{3}$$

with $t$ and $p$ being the ranks and components of the spherical harmonics $(Y_p^{t*})$, $\langle f\|C^{(2)}\|f\rangle = -1.366$, $\langle f\|C^{(4)}\|f\rangle = 1.128$, $\langle f\|C^{(6)}\|f\rangle = -1.27$, $\rho$ is the overlap integral between the valence subshells of the ligating atom and the 4f subshell of the lanthanide ion, $\beta = 1/(1 \pm \rho)$ is a parameter that defines the centroid of the electronic density, $g$ is the charge factor and $\alpha'$ is an effective polarizability from each ligand around the $Ln^{3+}$. In eq 2, the average energy denominator method[30,31] is used and also the simple overlap model (SOM) for the ligand field.[28,29] In eq 3, the bond overlap model (BOM) for the dynamic coupling mechanism is used.[27]

The overlap polarizabilities $\alpha_{OP}$ are quantities related to the covalent fraction of a chemical bond,[27,32−34] and it is given by

$$\alpha_{OP} = \frac{e^2\rho^2 R^2}{2\Delta\varepsilon} \tag{4}$$

where $e$ is the electron charge, $R$ is the length of the bond, and $\Delta\varepsilon$ is an excitation energy associated with the chemical bond.

The intensity parameters from the forced electric dipole mechanism $\Omega_K$ can be calculated using values of bond stretching force constants $k$ for both acceptor $\Omega_K^A$ and donor $\Omega_K^D$ lanthanides ions. These values can be obtained from DFT calculations, via displacements of the activator ion along each of its bonds.[35] The displacements result in collective-mode force constants (the so-called effective $k$, $k^{\text{eff}}$), where each value of $k^{\text{eff}}$ corresponds to simultaneous deformation of all bonds of the central atom. Decomposition of $k^{\text{eff}}$ into $k$ of the individual bonds is described in detail in a previous work.[35] Such technique requires $N_{\text{bonds}} \times 2N_{\text{steps}} + 1$ single point calculations, where $N_{\text{steps}}$ is number of steps in the displacement procedure and $N_{\text{bonds}}$ is the activator coordination number.

In the present work, we have assumed that bond force constants depend on bond length as $k = e^{(aR^2+bR+c)}$, where $R$ is bond length. It was found empirically that this particular function gives very good results. Given any set of displacements of the central atom, and treating the bonds as mechanical springs, total energy of such a set of springs can be calculated for $j$th displacement, as a sum of

$$E_i = E_0 + \sum_j \frac{k_j(\Delta R_{ij})^2}{2} \tag{5}$$

where $k_j$ is the force constant of the $j$th bond, $\Delta R_{ij}$ is the change in bond length of the $j$th bond under $i$th displacement, and $E_0$ is total energy when all $\Delta R_{ij}$ are zero, i.e., at the equilibrium position. Given the list of total energies from DFT for the same set of displacements, $k_j$ values can be obtained via least-squares fitting of the $a$, $b$, $c$, and $E_0$ parameters.

Here, we have used displacements of the central ion along the $x$, $y$, $z$ coordinate axes, resulting in $3 \times 2 N_{\text{steps}}$ single-point calculations. $N_{\text{steps}}$ was 2, meaning two steps in each direction: the central atom was displayed by $\pm 0.05$ Å and $\pm 0.1$ Å from its original position.

DFT calculations (using Elk,[36,37] see the charge factors calculations section in the Supporting Information for more details) were performed on the unmodified experimental geometry. It occurred that the central atom is located not at the energy minimum. The resulting force constants turn out to have scattered values, some of them even being negative. One possible workaround is optimization of every particular tested geometry. On the one hand, it is a lot of computational effort. On the other hand, the obtained force constants would correspond to each particular geometry only, i.e., would not be transferable.

Thus, we have modified the fitting procedure, adding $R_{0j}$ parameters (independent of $i$). The physical meaning is such that $j$th bond is deformed by $R_{0j}$ in respect to its equilibrium length. The $R_{0j}$ values effectively absorb errors and should be handled with care: too large values mean incorrect geometry. The initial displacement values can thus serve as a measure of quality of experimental geometry determination. On the bright side, such an approach is universal and must work with any geometry. With small $R_{0j}$, it results in very reasonable $k$. See the charge factor calculations section in the Supporting Information for the values of $k$ and $R_{0j}$. Finally, the charge factors in eq 2 can be calculated by[27,32]

$$g_j = R_j \sqrt{\frac{k_j}{2(\Delta \varepsilon)_j}} \tag{6}$$

where $\Delta \varepsilon$ is an excitation energy associated with the chemical bond, the same quantity that appears in eq 4.

**3.2. Energy Transfer Rates Involving Tb–Eu Ions.** The energy transfer rates between lanthanide ions were calculated taking into account the dipole–dipole ($W_{\text{d–d}}$), dipole–quadrupole ($W_{\text{d–q}}$), quadrupole–quadrupole ($W_{\text{q–q}}$), exchange ($W_{\text{ex}}$),[10] and magnetic dipole–magnetic dipole ($W_{\text{md–md}}$) mechanisms, eqs 7–11, respectively:

$$W_{\text{d–d}} = \frac{(1 - \sigma_1^{\text{D}})^2 (1 - \sigma_1^{\text{A}})^2}{[J_{\text{D}}^*][J_{\text{A}}]} \frac{4\pi}{3\hbar} \frac{e^4}{R_L^6} \left( \sum_K \Omega_K^{\text{D}} \langle \psi_{\text{D}} J_{\text{D}} \| U^{(K)} \| \psi_{\text{D}}^* J_{\text{D}}^* \rangle^2 \right)$$
$$\times \left( \sum_K \Omega_K^{\text{A}} \langle \psi_{\text{A}}^* J_{\text{A}}^* \| U^{(K)} \| \psi_{\text{A}} J_{\text{A}} \rangle^2 \right) F \tag{7}$$

$$W_{\text{d–q,q–d}} = \frac{(1 - \sigma_1^{\text{D,A}})^2 (1 - \sigma_2^{\text{A,D}})^2}{[J_{\text{D}}^*][J_{\text{A}}]} \frac{\pi e^4}{\hbar R_L^8} \langle f \| C^{(2)} \| f \rangle^2$$
$$\times \left[ \left( \sum_K \Omega_K^{\text{D}} \langle \psi_{\text{D}} J_{\text{D}} \| U^{(K)} \| \psi_{\text{D}}^* J_{\text{D}}^* \rangle^2 \right) \langle r^2 \rangle_{\text{A}}^2 \langle \psi_{\text{A}}^* J_{\text{A}}^* \| U^{(2)} \| \psi_{\text{A}} J_{\text{A}} \rangle^2 \right.$$
$$\left. + \left( \sum_K \Omega_K^{\text{A}} \langle \psi_{\text{A}} J_{\text{A}} \| U^{(K)} \| \psi_{\text{A}}^* J_{\text{A}}^* \rangle^2 \right) \langle r^2 \rangle_{\text{D}}^2 \langle \psi_{\text{D}} J_{\text{D}}^* \| U^{(2)} \| \psi_{\text{D}} J_{\text{D}} \rangle^2 \right]$$
$$\times F \tag{8}$$

$$W_{\text{q–q}} = \frac{(1 - \sigma_2^{\text{D}})^2 (1 - \sigma_2^{\text{A}})^2}{[J_{\text{D}}^*][J_{\text{A}}]} \frac{28\pi}{5\hbar} \frac{e^4}{R_L^{10}}$$
$$\times \langle r^2 \rangle_{\text{D}}^2 \langle r^2 \rangle_{\text{A}}^2 \langle f \| C^{(2)} \| f \rangle^4 \langle \psi_{\text{D}} J_{\text{D}} \| U^{(2)} \| \psi_{\text{D}}^* J_{\text{D}}^* \rangle^2$$
$$\times \langle \psi_{\text{A}}^* J_{\text{A}}^* \| U^{(2)} \| \psi_{\text{A}} J_{\text{A}} \rangle^2 F \tag{9}$$

$$W_{\text{ex}} = \frac{2\pi}{\hbar} \left[ \left( \frac{e^2}{R_L} \right) \rho_{f-f}^2 \right]^2 F \tag{10}$$

$$W_{\text{md–md}} = \frac{(1 - \sigma_1^{\text{D}})^2 (1 - \sigma_1^{\text{A}})^2}{[J_{\text{D}}^*][J_{\text{A}}]} \frac{4\pi}{3\hbar} \frac{\mu_B^4}{R_L^6} \langle \psi_{\text{D}} J_{\text{D}} \| L + 2S \| \psi_{\text{D}}^* J_{\text{D}}^* \rangle^2$$
$$\times \langle \psi_{\text{A}}^* J_{\text{A}}^* \| L + 2S \| \psi_{\text{A}} J_{\text{A}} \rangle^2 F \tag{11}$$

where the intensity parameters $\Omega_K$ are calculated from eq 1 using only the FED mechanism (eq 2), since in Kushida's expressions the appearance of the $\Omega_K$ parameters is due to opposite parity configuration mixing, by the odd components of the ligand field, like in the Judd-Ofelt theory.[13] In eq 8, the product $(1 - \sigma_1^{\text{D,A}})^2 (1 - \sigma_2^{\text{A,D}})^2$ is the same for both terms in the right-hand side. In the present work we calculated the values of $g$ (eq 6) using periodic DFT (unit cell-based, augmented plane-wave basis, PBEsol functional[38]), as described in section 3.1 and charge factors calculations section in the Supporting Information), while $\rho$ (Ln-oxygen overlap integral) was calculated for each Ln-O pair (Ln = Tb$^{3+}$ and Eu$^{3+}$) using molecule-like DFT (ADF,[39] BP86 functional[40,41]/TZ2P atomic orbitals basis,[42] and the inclusion of zero-order regular approximation (ZORA) to scalar relativistic effects[43–45]) leading to $\rho = 0.057$, 0.052, and 0.047 for Sr$_3$Tb(PO$_4$)$_3$, Sr$_{1.5}$Ba$_{1.5}$Tb(PO$_4$)$_3$, and Ba$_3$Tb(PO$_4$)$_3$, respectively. The sets of $\Omega_K$ (FED) values obtained, in units of $10^{-20}$ cm$^2$, are Tb$^{3+}$ {$\Omega_2$ = 0.595; $\Omega_4$ = 0.209; $\Omega_6$ = 0.263} and Eu$^{3+}$ {$\Omega_2$ = 0.821; $\Omega_4$ = 0.377; $\Omega_6$ = 0.518}. The $W_{\text{q–q}}$, $W_{\text{ex}}$, and $W_{\text{md–md}}$ mechanisms are independent of the $\Omega_K$ parameters. Noteworthy, only one set of $\Omega_K$ was obtained, while there are three compounds in question. On the one hand, the ET rate calculations for Sr$_3$Tb(PO$_4$)$_3$ showed that dipole–dipole and dipole–quadruple mechanism that require $\Omega_K$ have a negligible contribution to the total ET rate. On the other hand, there were somehow larger errors in the force constants of both Sr$_{1.5}$Ba$_{1.5}$Tb(PO$_4$)$_3$, and Ba$_3$Tb(PO$_4$)$_3$ (see the Supporting Information, Table S2). We have thus used the same (corresponding to the most reliable $\Omega_K$ set of the force constants) for the three compounds.

In eq 10, $\rho_{f-f}$ is the overlap integral between the 4f subshells of the donor and acceptor lanthanide ions. Figure S2 shows, for the case of Tb–Eu, the behavior of $\rho_{f-f}$ with the Tb–Eu distance ($R_L$). It is clear that $\rho_{f-f}$ decays very fast to zero with the increase of $R_L$. This is the reason why the rate $W_{\text{ex}}$ frequently can be neglected, mainly in diluted systems, in the Ln–Ln energy transfer processes, in contrast to the case of intramolecular energy transfer processes in lanthanide chelates.[8,10]

Nonradiative energy transfer involving magnetic dipole interactions in inorganic solids containing donor and acceptor ions has been treated in the early 1950s by Dexter,[9] and in the 1990s these interactions were applied to energy transfer between lanthanide ions, in inorganic crystals, by Tanner et al.[46–49] A demonstration of our formulation (eq 11, using data from Fano and Racah[50]) is presented in the magnetic dipole–

magnetic dipole energy transfer rate section in the Supporting Information.

In eqs 7–11, $\langle \psi J \| \| \psi^* J^* \rangle$ are doubly reduced matrix elements that depend only on the lanthanide ion: the matrix elements $\langle \psi J \| L+2S \| \psi^* J^* \rangle$ were calculated in the intermediate coupling scheme by using Ofelt's eigenfunctions,[51] and the $\langle \psi J \| U^{(K)} \| \psi^* J^* \rangle^2$ were taken from Carnall et al.[52] $\langle r^K \rangle$ are 4f radial integrals. The shielding factors $(1-\sigma_k)$ for donor and acceptor (with $k = 1$ and 2) are given by[53]

$$(1 - \sigma_k^{D,A}) = \rho(2\beta)^{k+1} \tag{12}$$

where $\rho$ and $\beta$ are the same quantities that appear in eqs 2–4. In eq 11, $\mu_B \left( = \frac{e\hbar}{2m_e c} \right)$ is the Bohr magneton.

$F$ is the spectral overlap factor that expresses the energy mismatch conditions which contains a sum over Franck–Condon factors. In the case of energy transfer between two lanthanide ions, the following analytical expression for $F$ has been used:[10]

$$F = \frac{\ln(2)}{\sqrt{\pi}} \frac{1}{\hbar^2 \gamma_D \gamma_A} \left\{ \left[ \left( \frac{1}{\hbar \gamma_D} \right)^2 + \left( \frac{1}{\hbar \gamma_A} \right)^2 \right] \ln(2) \right\}^{-1/2}$$

$$\times \exp \left[ \frac{1}{4} \frac{\left( \frac{2\Delta}{(\hbar \gamma_D)^2} \ln 2 \right)^2}{\left[ \left( \frac{1}{\hbar \gamma_A} \right)^2 + \left( \frac{1}{\hbar \gamma_D} \right)^2 \right] \ln 2} - \left( \frac{\Delta}{\hbar \gamma_D} \right)^2 \ln(2) \right] \tag{13}$$

where $\hbar \gamma_D$ and $\hbar \gamma_A$ correspond to the bandwidths at half-height (in erg) of the donor and acceptor, respectively. $\Delta$ is the energy difference between donor and acceptor transitions, $\Delta = E_D - E_A$. The spectral overlap factor $F$ is given in $erg^{-1}$.

The energy transfer mechanisms, pathways and their respective donor and acceptor states (Figures 1 and 2) were selected according to energy mismatch conditions and selection rules on the $J$ quantum numbers. These selection rules are for the multi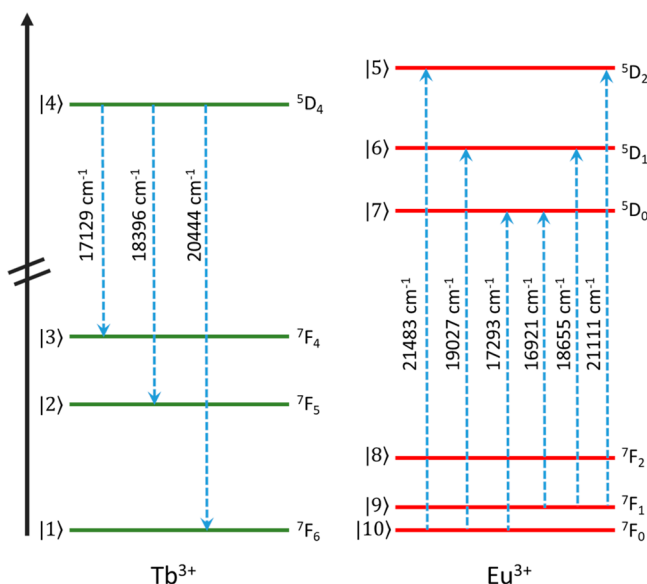polar mechanisms ($W_{d-d}$, $W_{d-q}$, and $W_{q-q}$) $|J - J'| \le K \le J + J'$; for the exchange mechanism ($W_{ex}$), the isotropic contribution, no defined selection rules on $J$ appear; for the magnetic dipole mechanism ($W_{md-md}$) $\Delta J = 0$, $\pm 1$. With exception of $W_{ex}$, $J = J' = 0$ is excluded, unless $J$-mixing effects are considered as in the present work.

The energy transfer rates were calculated by the sum over eqs 7–11 ($W = W_{d-d} + W_{d-q} + W_{q-q} + W_{ex} + W_{md-md}$) for each pathway under the following assumptions. (1) In the case of the acceptor $Eu^{3+}$ ion, the thermal populations of the $^7F_0$ (0.64) and the $^7F_1$ (0.33), at 300 K, were taken into account. In the case of the pathway involving the $^7F_0 \rightarrow {}^5D_0$ transition, the $J$-mixing between the $^7F_0$ and $^7F_2$ levels (of the order of 5%) was considered. (2) When $\Delta$ is negative (the donor state lies below the acceptor level), the energy transfer rates were multiplied by the barrier factor $e^{-\left( \frac{|\Delta|}{k_B T} \right)}$, where $k_B$ is Boltzmann's constant and $T$ is the temperature. Except in the case of pathway 9 ($^5D_4 \rightarrow {}^7F_5$ to $^7F_1 \rightarrow {}^5D_1$), where the electronic Stark levels are in perfect resonance conditions, as shown in Figure 3 and discussed by Berry et al.[54] (3) For each donor–acceptor distance $R_L$, $W$ is multiplied by the number of neighboring donor ($Tb^{3+}$) ions at that distance and divided by the total neighboring $Tb^{3+}$ donors.

Under these assumptions above, the average donor–acceptor energy transfer rate $\langle W \rangle$ (denoted also in literature as $k_{ET}$) is given by

$$\langle W \rangle = \sum_{j=1}^{3} \langle W \rangle_j = \xi_D \xi_A \sum_{j=1}^{3} \left( \frac{c_j W_j}{\sum_{i=1}^{3} c_i} \right) \tag{14}$$

where index $j$ represents the neighboring order (1st, 2nd, and 3rd, respectively), the coefficient $c$ ($c_1 = 3$, $c_2 = 2$, and $c_3 = 6$) is the number of nearest neighbors at the distance $R_L(j)$ (as will be shown in Table 1), and $W_j$ is the pairwise energy transfer rate for that distance. The site occupation probability $\xi$ is given by the relative mol % concentration. For the sake of clarification, in a compound of the type $Sr_3 Tb_{1-x} Eu_x (PO_4)_3$, as it will be used here, $\xi_D = 1-x$ and $\xi_A = x$. It is important to emphasize that these assumptions are consistent with the general treatment proposed by Grant[55] and discussed by Wright.[56] In 1984, Strek[57] discussed the concentration dependence of energy transfer rates and eq 14 above is consistent with his eq (20). Eq 14 to be used in the rate equations could be inappropriate for an average of energy transfer rates $\langle W \rangle$ over a sphere of neighbors, formed only by donors ($Tb^{3+}$), much larger than the one adopted here.

## 4. RESULTS AND DISCUSSION

**4.1. Crystal Structure.** Careful measurements of the powder XRD patterns showed that all the synthesized samples were single phase having the eulytite cubic structure (Figure 4) with the space group $I\overline{4}3d$. The results relative to the neat $Sr_3 Tb(PO_4)_3$ and $Ba_3 Tb(PO_4)_3$ crystalline materials have already been reported by Paterlini et al.[58] We also report a picture of the crystal structure, where one of the three possible orientation of the oxygen atoms [O(1)] is considered (Figure 5). In fact, the tetrahedral phosphate anion is disordered, as it occupies three different positions, one for each oxygen atom. Each of these atoms shows an occupation factor of 0.3333. Data for the mixed eulytite $Sr_{1.5} Ba_{1.5} Tb(PO_4)_3$ show that it is isostructural with the Sr and Ba analogues with $a = 10.2965(1)$ Å. The value of the lattice parameter of this compound is intermediate between the one of $Sr_3 Tb(PO_4)_3$ and $Ba_3 Tb$-



**Figure 1.** Schematic energy level diagram showing the energy levels of the donor ($Tb^{3+}$) and the acceptor ($Eu^{3+}$) involved in the energy transfer processes. Each level is represented by $|i\rangle$ ($i = 1, 2, ..., 10$). This labeling will be used in the rate equations section.

| Pathway Label | Donor transition | Acceptor transition |
|---|---|---|
| 1 | $^5D_4 \rightarrow {^7F_6}$ | $^7F_1 \rightarrow {^5D_0}$ |
| 2 | $^5D_4 \rightarrow {^7F_6}$ | $^7F_0 \rightarrow {^5D_0}$ |
| 3 | $^5D_4 \rightarrow {^7F_6}$ | $^7F_1 \rightarrow {^5D_1}$ |
| 4 | $^5D_4 \rightarrow {^7F_5}$ | $^7F_1 \rightarrow {^5D_0}$ |
| 5 | $^5D_4 \rightarrow {^7F_6}$ | $^7F_0 \rightarrow {^5D_1}$ |
| 6 | $^5D_4 \rightarrow {^7F_5}$ | $^7F_0 \rightarrow {^5D_0}$ |
| 7 | $^5D_4 \rightarrow {^7F_4}$ | $^7F_1 \rightarrow {^5D_0}$ |
| 8 | $^5D_4 \rightarrow {^7F_4}$ | $^7F_0 \rightarrow {^5D_0}$ |
| 9 | $^5D_4 \rightarrow {^7F_5}$ | $^7F_1 \rightarrow {^5D_1}$ |
| 10 | $^5D_4 \rightarrow {^7F_5}$ | $^7F_0 \rightarrow {^5D_1}$ |
| 11 | $^5D_4 \rightarrow {^7F_6}$ | $^7F_1 \rightarrow {^5D_2}$ |
| 12 | $^5D_4 \rightarrow {^7F_6}$ | $^7F_0 \rightarrow {^5D_2}$ |
| 13 | $^5D_4 \rightarrow {^7F_4}$ | $^7F_1 \rightarrow {^5D_1}$ |

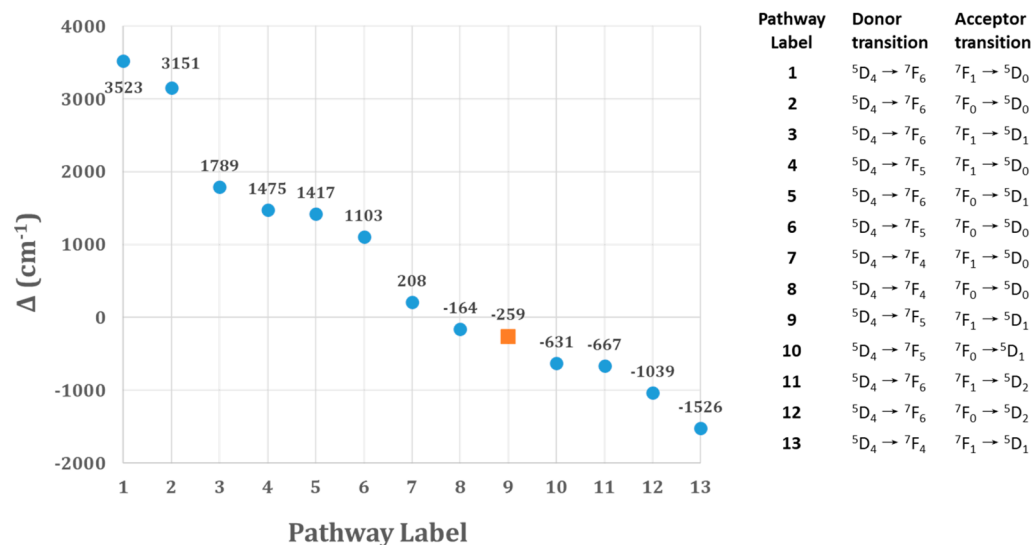**Figure 2.** Values of $\Delta$ (used in eq 13) for the selected energy transfer pathways. The highlighted point represents the energy transfer from $^5D_4 \rightarrow {^7F_5}$ to $^7F_1 \rightarrow {^5D_1}$ (pathway 9).
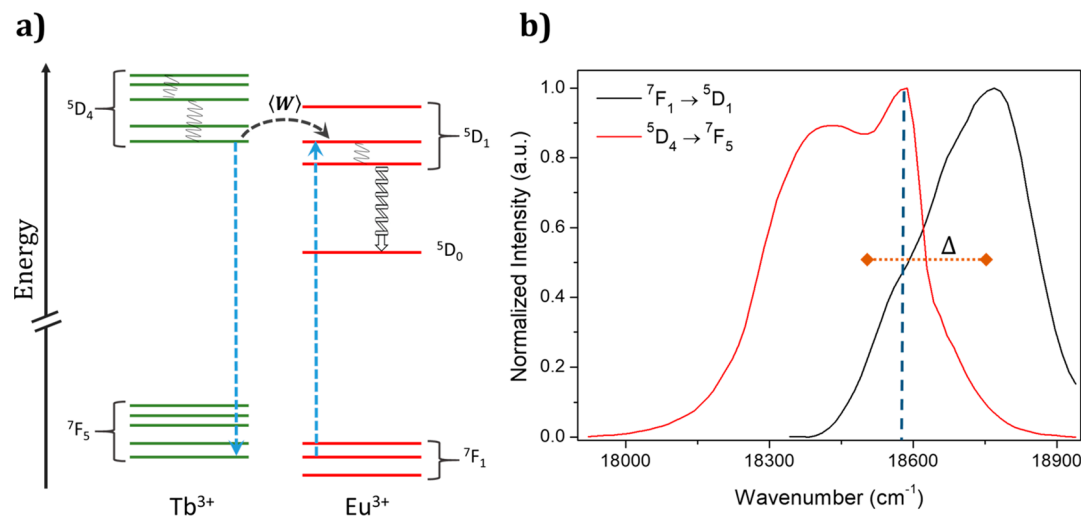
**Figure 3.** Pathway 9: (a) partial schematic energy level diagram for the $Tb^{3+}$ and $Eu^{3+}$ Stark levels. (b) The emission (red line) and absorption (black line) spectra of donor and acceptor, respectively. The dashed vertical line at 18580 $cm^{-1}$ represents the perfect resonance between Stark levels of the donor and acceptor levels. The dotted horizontal line represents the energy difference between the barycenters of the $^5D_4 \rightarrow {^7F_5}$ and $^7F_1 \rightarrow {^5D_1}$ transitions.

**Table 1. Distances between a Reference Cation and Nearest Neighbor Ones in the Eulytites under Investigation**

| | $Sr_3Tb(PO_4)_3$ Å (error) | $Sr_{1.5}Ba_{1.5}Tb(PO_4)_3$ Å (error) | $Ba_3Tb(PO_4)_3$ Å (error) |
|---|---|---|---|
| distance 1 ($\times 3$) | 3.971(2) | 4.041(3) | 4.121(2) |
| distance 2 ($\times 2$) | 4.378(1) | 4.459(1) | 4.537(1) |
| distance 3 ($\times 6$) | 4.754(1) | 4.841(3) | 4.923(3) |

$(PO_4)_3$. This agrees with the formation of a solid solution in the case of $Sr_{1.5}Ba_{1.5}Tb(PO_4)_3$. The gradual increase of the crystal cell passing from Sr- to Ba-based eulytite is clearly visible upon inspection of Figure 4. In fact, according to Bragg's law, this behavior is accompanied by a gradual shift of the peaks toward lower diffraction angles. Furthermore, there is only one site for both divalent and trivalent cations with

coordination number 9 and point symmetry $C_3$. The $A^{2+}/M^{3+}$ pairs of cations are disordered on a single crystallographic site with a relative occupation of 0.75/0.25. The lattice parameters are virtually unchanged upon partial substitution of $Tb^{3+}$ with $Eu^{3+}$ (doping) due to the similarity of the ionic radii (1.095 Å for $Tb^{3+}$ and 1.12 for $Eu^{3+}$ Å in 9-fold coordination).[59]

It is therefore clear that the substitution of $Sr^{2+}$ with the larger $Ba^{2+}$ ion does not, nor does $Eu^{3+}$ doping, modify the eulytite structure. On the other hand, the partial or complete replacement of $Sr^{2+}$ with the larger $Ba^{2+}$ increases the separation between $Tb^{3+}$ ions, and these distances of the 11 nearest neighboring cations from a reference $M^{3+}$ ion are reported in Table 1. Due to the occupation factors reported above, one $M^{3+}$ ion on average is surrounded by $11 \times 0.25 = 2.75$ $M^{3+}$ near neighbor ions. This implies that in the neat erbium eulytites, each $Tb^{3+}$ ion has 2.75 $Tb^{3+}$ nearest neighbors, and in the Tb,Eu-ones, 2.475 $Tb^{3+}$ and 0.275 $Eu^{3+}$ are nearest neighbor ions. In the presence of the $Eu^{3+}$
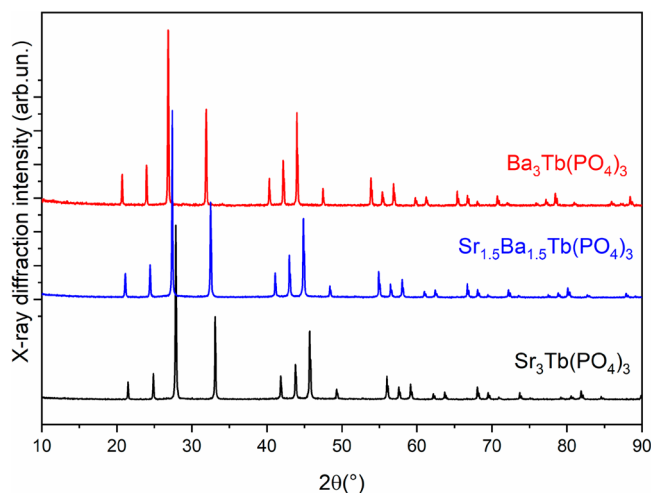
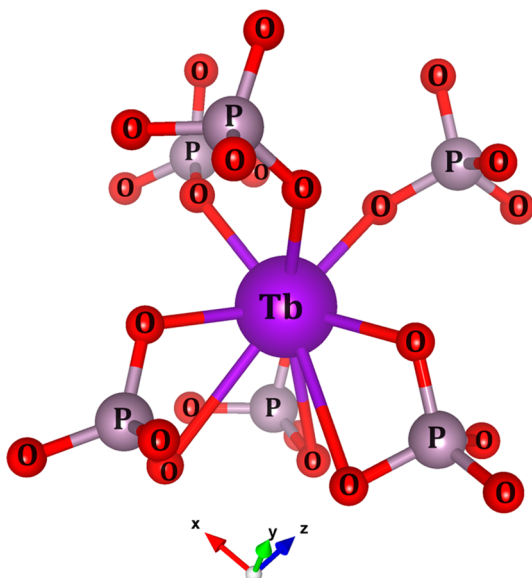**Figure 4.** XRD powder patterns of the compounds studied in this work.



**Figure 5.** Picture of the Eu/Tb/Sr surrounding from the crystal structure of $A_3Tb(PO_4)_3$, with A = Sr, Ba. Only atom O(1) with an occupancy factor of 0.3333 is depicted. Vertical is the $C_3$ symmetry axis. Similar pictures for O(2) and O(3) types are shown in Figure S1.

dopant, the crystallographic positions of the atoms are the same and so the distances of $Tb^{3+}-Tb^{3+}$ and $Tb^{3+}-Eu^{3+}$ are considered to be in practice identical.

These values suggest that presumably the ET efficiency will probably decrease in the Sr > (Sr,Ba) > Ba due to the longer D−A separation.

**4.2. Energy Transfer and Rate Equations.** The numerical results for the $Sr_3Tb_{0.90}Eu_{0.10}(PO_4)_3$ are shown in Tables 2, 3, and 4. The energy transfer rates for the other $Ba_3Tb_{0.90}Eu_{0.10}(PO_4)_3$ and $Sr_{1.5}Ba_{1.5}Tb0.90Eu_{0.10}(PO_4)_3$ eulytites are presented in Tables S3−S5 and Tables S6−S8, respectively. The behavior of $\rho_{f-f}$ is presented in Figure S2. By way of comparison, $\rho_{f-f}$ for a pair of Tb−Eu is slightly higher than for the pair Yb−Er at the same distance.[11] This is a manifestation of the lanthanide contraction since the pair Yb−Er has the 4f electronic density more contracted than the pair of Tb−Eu.

The first relevant theoretical conclusion we get from the transfer rate values in these tables is that, at least within the sphere containing the three nearest neighbors $Tb^{3+}$ ions (Table 2), the exchange ($W_{ex}$) mechanism is the dominant one. The quadrupole−quadrupole ($W_{q-q}$) mechanism becomes more important (in Tables 3 and 4 and also in the tables in the energy transfer rates for Ba and SrBa eulytites section in the Supporting Information) when the $R_L$ is higher than 4.12 Å. This is consistent with the conclusions of previous works.[10,11,20] It is worth noting that Dexter and Schulman[12] have given strong theoretical indication corroborating this conclusion for the case of donor−acceptor energy transfer involving electric dipole forbidden transitions. The relevance of the q-q mechanism for energy transfer between lanthanide ions occupying centrosymmetric sites in inorganic crystals was investigated earlier by Tanner et al.[49] (this reference was inadvertently missed and not quoted in a recent work by some of the present authors[11]). The major difference between the transfer rate expressions in Chua et al.[49] and in Carneiro Neto et al.[11] concerns the inclusion, in the transfer rates expressions, of the rather strong shielding effects on the 4f subshell due to the filled 5s and 5p subshells. In this context our theoretical treatment[11] does not take into account explicitly local field corrections, as in Chua et al.[49] and other earlier works,[9] since we consider that effects due to the medium containing donor and acceptor ions are, at least in part, implicitly accounted for through eq 14 relating the shielding factors to the overlap integral $\rho$ in the first coordination sphere. This is even more evident in the case of the exchange mechanism ($W_{ex}$) which is strongly dependent on the Ln−Ln overlap integral $\rho_{f-f}$ (Figure S2).

Since $W_{d-d}$, $W_{d-q}$, and $W_{md-md}$ values are negligible (they together contribute less than 0.16% of the total energy transfer rates, see Tables 2−4, S3−S5, and S6−S8), it is clearly expected that the contributions from the magnetic dipole-electric multipole ($W_{md-d}$ and $W_{md-q}$) mechanisms are also negligible.[9]

We will use the following rate equations model for the schematic level diagram shown in Figure 1. Our premises are the following: (i) the use of normalized populations $\eta$ ($0 \leq \eta \leq 1$) for both ensembles of donors and acceptors, $\eta$ represents fractions of the number of ions, in each ensemble, per unit volume ($N_D$ for donors and $N_A$ for acceptors); (ii) it will be assumed that the sample is uniformly illuminated and that in each ensemble the ions are equivalent independent of energy diffusion; (iii) the ground state energy levels of donors and acceptors are considered very little depleted under not very high excitation power and, when it is the case, their populations are equal to their thermal ones.

According to the above premises, the rate equation of the donor state $|4\rangle$ ($^5D_4$) can be written as

$$\frac{d\eta_4}{dt} = -\left(\frac{1}{\tau_4}\eta_4 + \langle W\rangle_{64}\eta_4 + \langle W\rangle_{14}\eta_4\right) + (\Phi\eta_H + \langle W\rangle_{14}\eta_4)$$

(15)

where $\Phi$ is an effective rate of population of the $^5D_4$, $\eta_H$ is the population of the host absorbing level, $\langle W\rangle_{64} \cong \langle W\rangle$ is the average donor−acceptor energy transfer rate calculated according to eq 14, and using the values in Tables 2, 3, and 4, $\tau_4$ is the lifetime of the $^5D_4$ in the absence of the $Eu^{3+}$ ion. Considering that $\Phi\eta_H$ contributes to the rise time of the transient of level $|4\rangle$ and since in the presence of $Eu^{3+}$ no rise time is observed (Figure 9), eq 15 is applied only to the decay

**Table 2. Pairwise Energy Transfer Rates ($s^{-1}$), for Each Mechanism, from $Tb^{3+}$ to $Eu^{3+}$ in $Sr_3Tb_{0.90}Eu_{0.10}(PO_4)_3$ for Donor–Acceptor Distance $R_L$ = 3.97 Å[a]**

| pathway label | donor | acceptor | $W_{d-d}$ | $W_{d-q}$ | $W_{q-q}$ | $W_{ex}$ | $W_{md-md}$ | $W$ |
|---|---|---|---|---|---|---|---|---|
| 1 | $^5D_4 \to {}^7F_6$ | $^7F_1 \to {}^5D_0$ | 0.00 | 0.00 | 0.00 | $6.56 \times 10^{-2}$ | 0.00 | $2.16 \times 10^{-2}$ |
| 2 | $^5D_4 \to {}^7F_6$ | $^7F_0 \to {}^5D_0$ | $4.00 \times 10^{-8}$ | $2.08 \times 10^{-5}$ | $1.95 \times 10^{-2}$ | $2.25 \times 10^{-1}$ | 0.00 | $3.91 \times 10^{-4}$ |
| 3 | $^5D_4 \to {}^7F_6$ | $^7F_1 \to {}^5D_1$ | $1.47 \times 10^{-4}$ | $7.63 \times 10^{-2}$ | $7.17 \times 10^1$ | $3.17 \times 10^3$ | 0.00 | $1.07 \times 10^3$ |
| 4 | $^5D_4 \to {}^7F_5$ | $^7F_1 \to {}^5D_0$ | 0.00 | 0.00 | 0.00 | $3.40 \times 10^2$ | $1.91 \times 10^{-1}$ | $1.12 \times 10^2$ |
| 5 | $^5D_4 \to {}^7F_6$ | $^7F_0 \to {}^5D_1$ | $5.74 \times 10^{-4}$ | $2.98 \times 10^{-1}$ | $2.80 \times 10^2$ | $1.24 \times 10^4$ | 0.00 | $4.18 \times 10^3$ |
| 6 | $^5D_4 \to {}^7F_5$ | $^7F_0 \to {}^5D_0$ | $5.22 \times 10^{-4}$ | $3.57 \times 10^{-1}$ | $4.51 \times 10^2$ | $3.29 \times 10^2$ | 0.00 | 1.25 |
| 7 | $5D_4 \to {}^7F_4$ | $^7F_1 \to {}^5D_0$ | 0.00 | 0.00 | 0.00 | $1.43 \times 10^5$ | 1.08 | $4.72 \times 10^4$ |
| 8 | $^5D_4 \to {}^7F_4$ | $^7F_0 \to {}^5D_0$ | $2.77 \times 10^{-2}$ | 9.88 | $3.31 \times 10^3$ | $1.72 \times 10^5$ | 0.00 | $1.28 \times 10^2$ |
| **9** | $\mathbf{^5D_4 \to {}^7F_5}$ | $\mathbf{^7F_1 \to {}^5D_1}$ | $\mathbf{6.56 \times 10^{-2}}$ | $\mathbf{4.49 \times 10^1}$ | $\mathbf{5.67 \times 10^4}$ | $\mathbf{1.59 \times 10^5}$ | $\mathbf{7.18 \times 10^{-1}}$ | $\mathbf{7.12 \times 10^4}$ |
| 10 | $^5D_4 \to {}^7F_5$ | $^7F_0 \to {}^5D_1$ | 0.00 | 0.00 | 0.00 | $3.38 \times 10^4$ | $1.33 \times 10^1$ | $1.05 \times 10^3$ |
| 11 | $^5D_4 \to {}^7F_6$ | $^7F_1 \to {}^5D_2$ | 0.00 | 0.00 | 0.00 | $7.36 \times 10^4$ | 0.00 | $9.92 \times 10^2$ |
| 12 | $^5D_4 \to {}^7F_6$ | $^7F_0 \to {}^5D_2$ | $5.52 \times 10^{-3}$ | 2.87 | $2.69 \times 10^3$ | $3.10 \times 10^4$ | 0.00 | $1.48 \times 10^2$ |
| 13 | $^5D_4 \to {}^7F_4$ | $^7F_1 \to {}^5D_1$ | $1.05 \times 10^{-4}$ | $3.75 \times 10^{-2}$ | $1.26 \times 10^1$ | $2.50 \times 10^3$ | $1.52 \times 10^{-4}$ | $5.51 \times 10^{-1}$ |

$\langle W_1 \rangle = 3.09 \times 10^3 \ s^{-1}$

[a] $W$ is the sum over all mechanisms considering the assumptions (1) and (2) above. $\langle W \rangle_1$ is obtained by the sum of all $W$ values and applying this in eq 14 taking into consideration the assumption (3). One should notice that pathway 9 (highlighted in bold) is the dominant one and does not include the barrier factor as explained in the text.

**Table 3. Pairwise Energy Transfer Rates ($s^{-1}$), for Each Mechanism, from $Tb^{3+}$ to $Eu^{3+}$ in $Sr_3Tb_{0.90}Eu_{0.10}(PO_4)_3$ for Donor–Acceptor Distance $R_L$ = 4.38 Å[a]**

| pathway label | donor | acceptor | $W_{d-d}$ | $W_{d-q}$ | $W_{q-q}$ | $W_{ex}$ | $W_{md-md}$ | $W$ |
|---|---|---|---|---|---|---|---|---|
| 1 | $^5D_4 \to {}^7F_6$ | $^7F_1 \to {}^5D_0$ | 0.00 | 0.00 | 0.00 | $2.75 \times 10^{-4}$ | 0.00 | $9.06 \times 10^{-5}$ |
| 2 | $^5D_4 \to {}^7F_6$ | $^7F_0 \to {}^5D_0$ | $2.23 \times 10^{-8}$ | $9.52 \times 10^{-6}$ | $7.36 \times 10^{-3}$ | $9.42 \times 10^{-4}$ | 0.00 | $1.33 \times 10^{-5}$ |
| 3 | $^5D_4 \to {}^7F_6$ | $^7F_1 \to {}^5D_1$ | $8.18 \times 10^{-5}$ | $3.49 \times 10^{-2}$ | $2.70 \times 10^1$ | $1.33 \times 10^1$ | 0.00 | $1.331 \times 10^1$ |
| 4 | $^5D_4 \to {}^7F_5$ | $^7F_1 \to {}^5D_0$ | 0.00 | 0.00 | 0.00 | 1.42 | $1.06 \times 10^{-1}$ | $5.05 \times 10^{-1}$ |
| 5 | $^5D_4 \to {}^7F_6$ | $^7F_0 \to {}^5D_1$ | $3.20 \times 10^{-4}$ | $1.36 \times 10^{-1}$ | $1.06 \times 10^2$ | $5.18 \times 10^1$ | 0.00 | $5.20 \times 10^1$ |
| 6 | $^5D_4 \to {}^7F_5$ | $^7F_0 \to {}^5D_0$ | $2.90 \times 10^{-4}$ | $1.64 \times 10^{-1}$ | $1.70 \times 10^2$ | 1.38 | 0.00 | $2.74 \times 10^{-1}$ |
| 7 | $^5D_4 \to {}^7F_4$ | $^7F_1 \to {}^5D_0$ | 0.00 | 0.00 | 0.00 | $5.99 \times 10^2$ | $6.02 \times 10^{-1}$ | $1.98 \times 10^2$ |
| 8 | $^5D_4 \to {}^7F_4$ | $^7F_0 \to {}^5D_0$ | $1.54 \times 10^{-2}$ | 4.53 | $1.25 \times 10^3$ | $7.19 \times 10^2$ | 0.00 | 1.44 |
| **9** | $\mathbf{^5D_4 \to {}^7F_5}$ | $\mathbf{^7F_1 \to {}^5D_1}$ | $\mathbf{3.65 \times 10^{-2}}$ | $\mathbf{2.06 \times 10^1}$ | $\mathbf{2.14 \times 10^4}$ | $\mathbf{6.65 \times 10^2}$ | $\mathbf{4.00 \times 10^{-1}}$ | $\mathbf{7.28 \times 10^3}$ |
| 10 | $^5D_4 \to {}^7F_5$ | $^7F_0 \to {}^5D_1$ | 0.00 | 0.00 | 0.00 | $1.42 \times 10^2$ | 7.41 | 4.62 |
| 11 | $^5D_4 \to {}^7F_6$ | $^7F_1 \to {}^5D_2$ | 0.00 | 0.00 | 0.00 | $3.08 \times 10^2$ | 0.00 | 4.15 |
| 12 | $^5D_4 \to {}^7F_6$ | $^7F_0 \to {}^5D_2$ | $3.07 \times 10^{-3}$ | 1.31 | $1.02 \times 10^3$ | $1.30 \times 10^2$ | 0.00 | 5.03 |
| 13 | $^5D_4 \to {}^7F_4$ | $^7F_1 \to {}^5D_1$ | $5.86 \times 10^{-5}$ | $1.72 \times 10^{-2}$ | 4.74 | $1.05 \times 10^1$ | $8.48 \times 10^{-5}$ | $3.33 \times 10^{-3}$ |

$\langle W \rangle_2 = 1.24 \times 10^2 \ s^{-1}$

[a] $W$ is the sum over all mechanisms considering the assumptions 1) and 2) above. $\langle W \rangle_2$ is obtained by the sum of all $W$ values and applying this in Eq. 14 taking into consideration the assumption 3). One should notice that pathway 9 (highlighted in bold) is the dominant one and does not include the barrier factor as explained in the text.

part of the transient curve. This means that the term $\Phi \eta_H$ can be neglected in eq 15. Also, it may be seen that the negative and positive parts of the diffusion term $\langle W \rangle_{14} \eta_4$ cancel. Then, in the steady-state regime, solving eq 15 for $\eta_4$ leads to an average decay lifetime $\tau$ given by

$$\langle W \rangle = \frac{1}{\tau} - \frac{1}{\tau_4} \tag{16}$$

where $\tau$ is the measured lifetime in the presence of the $Eu^{3+}$ ion.

**4.3. Luminescence Spectroscopy.** Excitation and emission spectra for the 10% $Eu^{3+}$ doped compared with the undoped samples are shown in Figures 6 and 7, respectively, for the ($Sr^{2+}$, $Ba^{2+}$) eulytite as a representative example. The spectra for the other materials are similar and have been reported previously.[58] The excitation spectrum of the doped compound presents additional bands due to the europium ion, while the emission spectra are clearly different in the two cases:

in the undoped sample, only terbium bands are visible, while both $Tb^{3+}$ and $Eu^{3+}$ features appear in the doped one upon $Tb^{3+}$ excitation, demonstrating the presence of energy transfer of the type $Tb^{3+} \to Eu^{3+}$. This process is well documented in the literature, both in the case of one step donor–acceptor transfer[60] and in the case of transfer of excitation assisted by migration in the donor subset.[9] Upon excitation in the $^5D_3$ level of $Tb^{3+}$ or in the levels above it, the $^5D_4$ level is very rapidly populated by the cross-relaxation pathway of the type $^5D_3 + {}^7F_6 \to {}^5D_4 + ({}^7F_0, {}^7F_1)$.[15] The $^5D_4$ ($Tb^{3+}$) → $^5D_0$ ($Eu^{3+}$) transfer is operative through various mechanisms as described above and in the previous literature.[3,61]

By comparing the emission spectra of the three doped samples normalized with respect to the integrated intensity of the $^5D_4 \to {}^7F_5$ emission band of $Tb^{3+}$ around 545 nm, a decrease of the intensities of $Eu^{3+}$ bands with increasing D–A separation is clearly observed (Figure 8). This result indicates that the ET efficiency depends on the nature of the divalent

**Table 4. Pairwise Energy Transfer Rates ($s^{-1}$), for Each Mechanism, from $Tb^{3+}$ to $Eu^{3+}$ in $Sr_3Tb_{0.90}Eu_{0.10}(PO_4)_3$ for Donor–Acceptor Distance $R_L$ = 4.75 Å[a]**

| pathway label | donor | acceptor | $W_{d-d}$ | $W_{d-q}$ | $W_{q-q}$ | $W_{ex}$ | $W_{md-md}$ | $W$ |
|---|---|---|---|---|---|---|---|---|
| 1 | $^5D_4 \rightarrow {}^7F_6$ | $^7F_1 \rightarrow {}^5D_0$ | 0.00 | 0.00 | 0.00 | $1.15 \times 10^{-6}$ | 0.00 | $3.80 \times 10^{-7}$ |
| 2 | $^5D_4 \rightarrow {}^7F_6$ | $^7F_0 \rightarrow {}^5D_0$ | $1.36 \times 10^{-8}$ | $4.92 \times 10^{-6}$ | $3.23 \times 10^{-3}$ | $3.95 \times 10^{-6}$ | 0.00 | $5.18 \times 10^{-6}$ |
| 3 | $^5D_4 \rightarrow {}^7F_6$ | $^7F_1 \rightarrow {}^5D_1$ | $4.99 \times 10^{-5}$ | $1.81 \times 10^{-2}$ | $1.19 \times 10^1$ | $5.57 \times 10^{-2}$ | 0.00 | 3.94 |
| 4 | $^5D_4 \rightarrow {}^7F_5$ | $^7F_1 \rightarrow {}^5D_0$ | 0.00 | 0.00 | 0.00 | $5.97 \times 10^{-3}$ | $6.49 \times 10^{-2}$ | $2.34 \times 10^{-2}$ |
| 5 | $^5D_4 \rightarrow {}^7F_6$ | $^7F_0 \rightarrow {}^5D_1$ | $1.95 \times 10^{-4}$ | $7.06 \times 10^{-2}$ | $4.63 \times 10^1$ | $2.18 \times 10^{-1}$ | 0.00 | $1.54 \times 10^1$ |
| 6 | $^5D_4 \rightarrow {}^7F_5$ | $^7F_0 \rightarrow {}^5D_0$ | $1.77 \times 10^{-4}$ | $8.47 \times 10^{-2}$ | $7.46 \times 10^1$ | $5.79 \times 10^{-3}$ | 0.00 | $1.19 \times 10^{-1}$ |
| 7 | $^5D_4 \rightarrow {}^7F_4$ | $^7F_1 \rightarrow {}^5D_0$ | 0.00 | 0.00 | 0.00 | 2.51 | $3.67 \times 10^{-1}$ | $9.51 \times 10^{-1}$ |
| 8 | $^5D_4 \rightarrow {}^7F_4$ | $^7F_0 \rightarrow {}^5D_0$ | $9.41 \times 10^{-3}$ | $9.41 \times 10^{-3}$ | $5.48 \times 10^2$ | 3.02 | 0.00 | $4.01 \times 10^{-1}$ |
| **9** | $\mathbf{^5D_4 \rightarrow {}^7F_5}$ | $\mathbf{^7F_1 \rightarrow {}^5D_1}$ | $\mathbf{2.23 \times 10^{-2}}$ | $\mathbf{1.06 \times 10^1}$ | $\mathbf{9.38 \times 10^3}$ | **2.79** | $\mathbf{2.44 \times 10^{-1}}$ | $\mathbf{3.10 \times 10^3}$ |
| 10 | $^5D_4 \rightarrow {}^7F_5$ | $^7F_0 \rightarrow {}^5D_1$ | 0.00 | 0.00 | 0.00 | $5.94 \times 10^{-1}$ | 4.52 | $1.59 \times 10^{-1}$ |
| 11 | $^5D_4 \rightarrow {}^7F_6$ | $^7F_1 \rightarrow {}^5D_2$ | 0.00 | 0.00 | 0.00 | 1.29 | 0.00 | $1.74 \times 10{-2}$ |
| 12 | $^5D_4 \rightarrow {}^7F_6$ | $^7F_0 \rightarrow {}^5D_2$ | $1.88 \times 10^{-3}$ | $6.79 \times 10^{-1}$ | $4.45 \times 10^2$ | $5.45 \times 10^{-1}$ | 0.00 | 1.96 |
| 13 | $^5D_4 \rightarrow {}^7F_4$ | $^7F_1 \rightarrow {}^5D_1$ | $3.57 \times 10^{-5}$ | $8.89 \times 10^{-3}$ | 2.08 | $4.40 \times 10^{-2}$ | $5.17 \times 10^{-5}$ | $4.67 \times 10^{-4}$ |

$\langle W \rangle_3$ = $1.53 \times 10^2$ $s^{-1}$

[a]$W$ is the sum over all mechanisms considering the assumptions (1) and (2) above. $W_3$ is obtained by the sum of all $W$ values and applying this in eq 14 taking into consideration assumption (3). One should notice that pathway 9 (highlighted in bold) is the dominant one and does not include the barrier factor as explained in the text.
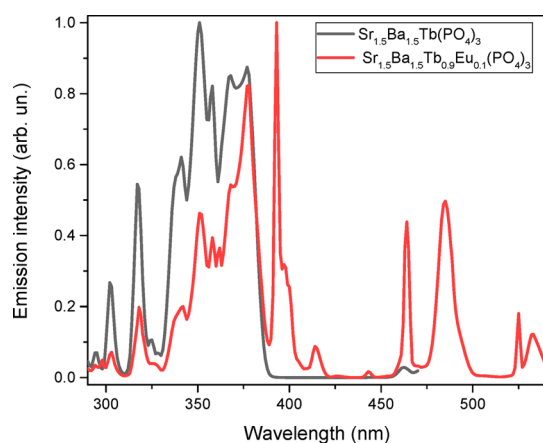


**Figure 6.** Room temperature excitation spectra of $Sr_{1.5}Ba_{1.5}Tb(PO_4)_3$ both with and without $Eu^{3+}$. Spectra were acquired by monitoring the emission at 542 nm for the undoped sample and at 611 nm for the doped one.
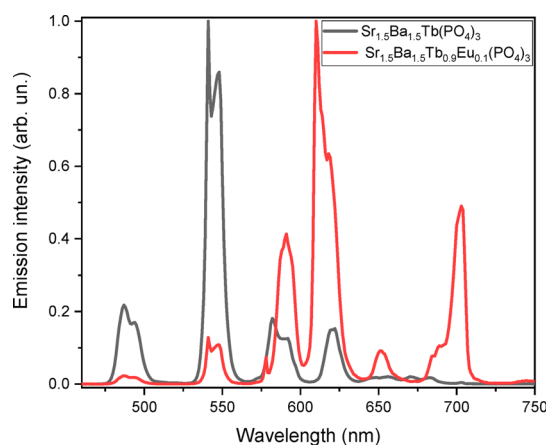


**Figure 8.** Comparison of the emission intensities of the $A_3Tb(PO_4)_3$ materials doped with $Eu^{3+}$. The spectral profiles were obtained upon excitation in $Tb^{3+}$ $^5D_3$ level and have been normalized with respect to the integrated intensity of the $^5D_4 \rightarrow {}^7F_5$ emission band of $Tb^{3+}$ around 545 nm.



**Figure 7.** Room temperature emission spectra of $Sr_{1.5}Ba_{1.5}Tb(PO_4)_3$ both with and without $Eu^{3+}$. Both spectra were acquired upon excitation at 351 nm.
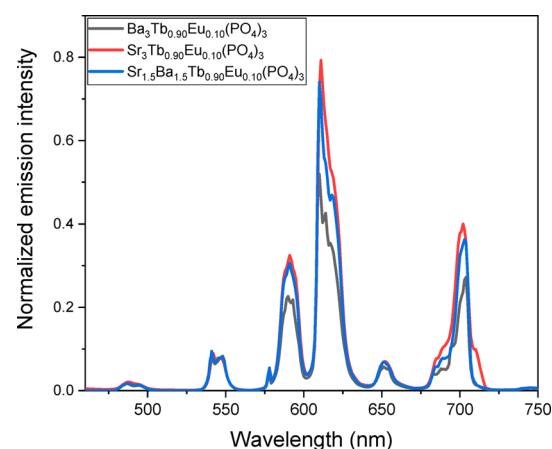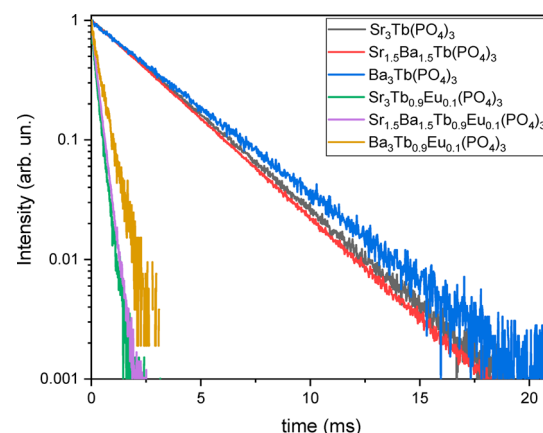


**Figure 9.** Room temperature decay curves of the $^5D_4$ luminescence in the eulytites under investigation. Excitation wavelength: 351 nm; emission wavelength: 541 nm.

**Table 5. $^5D_4$ Decay Times and Constants, Effective Energy Transfer Rates $\langle W \rangle$ between $Tb^{3+}$ and $Eu^{3+}$, and Energy Transfer Efficiencies $\eta_{ET}$ in the Tb-Based Eulytites under Investigation**

| material | x(Ba) | $\tau$ ($^5D_4$) (ms) | $1/\tau$ ($s^{-1}$) | $\langle W \rangle$ ($s^{-1}$) | $\eta_{ET}$ |
|---|---|---|---|---|---|
| $Sr_3Tb(PO_4)_3$ | 0 | 2.68 | $3.73 \times 10^2$ | – | – |
| $Sr_3Tb_{0.90}Eu_{0.10}(PO_4)_3$ | | 0.20 | $5.00 \times 10^3$ | $4.63 \times 10^3$ | 0.93 |
| $Sr_{1.5}Ba_{1.5}Tb(PO_4)_3$ | 0.5 | 2.60 | $3.85 \times 10^2$ | – | – |
| $Sr_{1.5}Ba_{1.5}Tb_{0.90}Eu_{0.10}(PO_4)_3$ | | 0.27 | $3.70 \times 10^3$ | $3.32 \times 10^3$ | 0.90 |
| $Ba_3Tb(PO_4)_3$ | 1 | 3.05 | $3.28 \times 10^2$ | – | – |
| $Ba_3Tb_{0.90}Eu_{0.10}(PO_4)_3$ | | 0.39 | $2.56 \times 10^3$ | $2.23 \times 10^3$ | 0.87 |

**Table 6. Experimental and total theoretical energy transfer rates from the $^5D_4$ level of the donor $Tb^{3+}$ ion to the $Eu^{3+}$ ion in the $Sr_3Tb_{0.90}Eu_{0.10}(PO_4)_3$, $Ba_3Tb_{0.90}Eu_{0.10}(PO_4)_3$, and mixed $Sr_{1.5}Ba_{1.5}Tb_{0.90}Eu_{0.10}(PO_4)_3$ eulytites**

| material | energy transfer rate ($s^{-1}$) | |
|---|---|---|
| | experimental | theoretical |
| $Sr_3Tb_{0.90}Eu_{0.10}(PO_4)_3$ | $4.63 \times 10^3$ | $3.37 \times 10^3$ |
| $Sr_{1.5}Ba_{1.5}Tb_{0.90}Eu_{0.10}(PO_4)_3$ | $3.32 \times 10^3$ | $1.48 \times 10^3$ |
| $Ba_3Tb_{0.90}Eu_{0.10}(PO_4)_3$ | $2.23 \times 10^3$ | $0.59 \times 10^3$ |

cations present in the materials and, as a consequence, on the distance between neighboring lanthanide ions.

Luminescence decay curves were collected for all prepared samples by monitoring the emission from the $^5D_4$ level of $Tb^{3+}$ (Figure 9). The decay profiles were found to be in all cases almost exponential. The presence of $Eu^{3+}$ strongly decreases the $Tb^{3+}$ decay constants with respect to the undoped samples, for all three $Sr^{2+}/Ba^{2+}$ compositions under investigation (Table 5). These observations indicate that the energy transfer to $Eu^{3+}$ is preceded by fast energy migration, as previously observed in other cases.[3,15] In order to estimate the ET efficiency $\eta_{ET}$ from the $^5D_4$ level, the following equation was used:

$$\eta_{ET} = 1 - \frac{\tau_{Tb-Eu}}{\tau_{Tb}} \qquad (17)$$

where $\tau_{Tb-Eu}$ and $\tau_{Tb}$ are the decay times of $^5D_4$ in the presence and in the absence of $Eu^{3+}$, respectively. The obtained values are reported in Table 5 and Figure S3. They show a decrease with increasing $Ba^{2+}$ content, demonstrating that the nature of the cation plays a role in the ET process.

The same effect was found for the average energy transfer rate $\langle W \rangle$, defined as

$$\langle W \rangle \cong \langle W \rangle_{64} = \frac{1}{\tau_{Tb-Eu}} - \frac{1}{\tau_{Tb}} \qquad (18)$$

and the resulting values, for both experimental and theoretical, are also reported in Table 6. The energy transfer rates and efficiencies depend on the interionic distances, which decrease moving from the Ba to the (Sr,Ba) and finally to the Sr-eulytite one.

The results for the $Ba_3Tb_{0.90}Eu_{0.10}(PO_4)_3$ material were obtained following the same procedures as for the $Sr_3Tb_{0.90}Eu_{0.10}(PO_4)_3$ one. Since the average distance in the Ba case is larger than in the Sr case, the total theoretical transfer rate is smaller in the former case, in agreement with the experimental one. Figure 10b shows the relative contributions of the two main mechanisms (exchange and quadrupole−quadrupole) for the Tb−Eu energy transfer process in $Sr_{3(1−x)}Ba_{3x}Tb_{0.90}Eu_{0.10}(PO_4)_3$ materials. The $W_{ex}$ contribution decreases faster than the $W_{q−q}$ one when the Tb−Eu distance increases. The contributions from the first neighboring cations (shortest distances) are by far the most important ones, as shown in Figure 10a.

The backward energy transfer from the acceptor ($Eu^{3+}$) to the donor ($Tb^{3+}$) is certainly operative, particularly considering that the lifetime of the $^7F_5$ level of the $Tb^{3+}$ ion is curiously abnormally high.[62−64] However, from the data in Figures 2 and 3 and the relative energy position of the $^5D_4$ ($Tb^{3+}$) level, it is not difficult to realize that the overall energy backward transfer (acceptor → donor) should be much less important than the overall forward transfer. The quantitative balance between these two processes would require a detailed solution and analysis of an appropriate system of rate equations in order to describe the transient of the $^5D_4$ ($Tb^{3+}$) level, a point which is outside the scope of the present work.
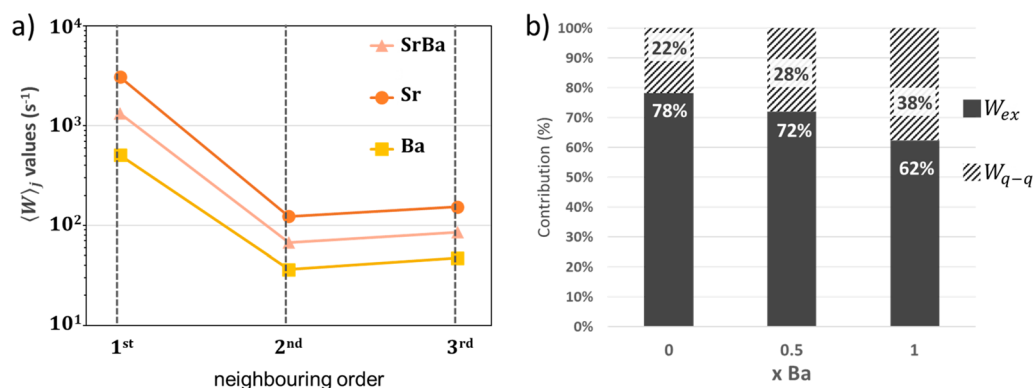


**Figure 10.** (a) Values of $\langle W_j \rangle$ obtained by eq 14 to each neighboring order. The 3rd neighbors have a little bit higher values than the 2nd ones for the reason that there are more donor ions ($c_3 = 6$ and $c_2 = 2$, respectively). (b) Relevant contributions of the $W_{q−q}$ and $W_{ex}$ mechanisms in the total energy transfer rates for each amount of $Ba^{2+}$ in $Sr_{3(1−x)}Ba_{3x}Tb_{0.90}Eu_{0.10}(PO_4)_3$ eulytite materials.

## 5. CONCLUSIONS

This work presented a deep study on the energy transfer processes in three eulytites with the composition $Sr_{3-x}Ba_xTb_{0.90}Eu_{0.10}(PO_4)$ ($x = 0, 0.5, 1$) by experimental and theoretical points of view; both approaches reach an agreement between them. From the experimental side, the effect of the divalent cation ($Sr^{2+}$ and $Ba^{2+}$) in the composition of the eulytite plays a key role to change the donor−acceptor distances and, consequently, the Tb−Eu energy transfer. From the theoretical part, it was proposed, for the first time, a new model to estimate the average of the energy transfer rates according to the neighboring donors and taking into consideration the proportion of donors/acceptors species.

Besides the good agreement between the experimental and theoretical approaches, it was noticed that the exchange mechanism is the predominant one for the overall Tb−Eu energy transfer process at least for distances not higher than 4.12 Å. This distance coincides with the first neighboring in the case of the $Ba_3Tb_{0.90}Eu_{0.10}(PO_4)_3$ eulytite. The quadrupole−quadrupole mechanism becomes the most relevant starting from the second neighboring donors where the shortest donor−acceptor distances are 4.38 Å ($Sr_3Tb_{0.90}Eu_{0.10}(PO_4)_3$ eulytite). This fact has been discussed on the basis of eqs 7−11. However, the energy transfer rates by the shortest donor−acceptor distance (1st neighboring order in Figure 10a) are dominant for the total $<W>$ (eq 14).

## ASSOCIATED CONTENT

### Supporting Information

The Supporting Information is available free of charge at https://pubs.acs.org/doi/10.1021/acs.jpcc.0c00759.

Theoretical details about the magnetic dipole−magnetic dipole energy transfer rate, the description of the computational procedures (calculations of charge factors and overlap integrals), and tables relative to the energy transfer rates for Ba and SrBa eulytites (PDF)

## AUTHOR INFORMATION

### Corresponding Authors

**Marco Bettinelli** − *Luminescent Materials Laboratory, Department of Biotechnology, University of Verona and INSTM, UdR Verona, 37134 Verona, Italy;* orcid.org/0000-0002-1271-4241; Email: marco.bettinelli@univr.it

**Oscar L. Malta** − *Department of Fundamental Chemistry, Federal University of Pernambuco, 50740-560 Recife, Brazil;* Email: oscar.malta@ufpe.br

### Authors

**Albano N. Carneiro Neto** − *Physics Department and CICECO − Aveiro Institute of Materials, University of Aveiro, 3810-193 Aveiro, Portugal;* orcid.org/0000-0003-2432-0992

**Renaldo T. Moura Jr.** − *Department of Chemistry and Physics, Federal University of Paraíba, 58397-000 Areia, Brazil;* orcid.org/0000-0002-8151-1640

**Andrii Shyichuk** − *Faculty of Chemistry, University of Wrocław, 50-383 Wrocław, Poland;* orcid.org/0000-0003-3174-2595

**Veronica Paterlini** − *Luminescent Materials Laboratory, Department of Biotechnology, University of Verona and INSTM, UdR Verona, 37134 Verona, Italy; Stockholm University, Department of Materials and Environmental Chemistry, 106 91 Stockholm, Sweden*

**Fabio Piccinelli** − *Luminescent Materials Laboratory, Department of Biotechnology, University of Verona and INSTM, UdR Verona, 37134 Verona, Italy;* orcid.org/0000-0003-0349-1960

Complete contact information is available at:
https://pubs.acs.org/10.1021/acs.jpcc.0c00759

### Notes

The authors declare no competing financial interest.

## REFERENCES

(1) *Energy transfer processes in condensed matter*; Di Bartolo, B., Ed.; Springer US: Boston, MA, 1984.

(2) Li, T.; Li, P.; Wang, Z.; Xu, S.; Bai, Q.; Yang, Z. A series of tunable emission phosphors of $Sm^{3+}$, $Eu^{3+}$ and $Mn^{2+}$ doped $Ba_3Tb(PO_4)_3$: luminescence and energy transfer. *RSC Adv.* **2015**, 5, 71735−71742.

(3) Carrasco, I.; Piccinelli, F.; Bettinelli, M. Luminescence of Tb-based materials doped with $Eu^{3+}$: case studies for energy transfer processes. *J. Lumin.* **2017**, 189, 71−77.

(4) Brites, C. D. S.; Millán, A.; Carlos, L. D. In *Handbook on the physics and chemistry of rare earths*; Pecharsky, V., Bünzli, J.-C. G., Eds.; Elsevier, Amsterdam, 2016; Vol. 49, pp 339−427.

(5) Bao, G.; Wong, K.-L.; Jin, D.; Tanner, P. A. A stoichiometric terbium-europium dyad molecular thermometer: energy transfer properties. *Light: Sci. Appl.* **2018**, 7, 96.

(6) Bünzli, J.-C. G. On the design of highly luminescent lanthanide complexes. *Coord. Chem. Rev.* **2015**, 293−294, 19−47.

(7) Tanner, P. A.; Zhou, L.; Duan, C.; Wong, K.-L. Misconceptions in electronic energy transfer: bridging the gap between chemistry and physics. *Chem. Soc. Rev.* **2018**, 47, 5234−5265.

(8) Carneiro Neto, A. N.; Teotonio, E. E. S.; de Sá, G. F.; Brito, H. F.; Legendziewicz, J.; Carlos, L. D.; Felinto, M. C. F. C.; Gawryszewska, P.; Moura, Jr., R. T.; Longo, R. L.; Faustino, W. M.; Malta, O. L. In *Handbook on the physics and chemistry of rare earths*; Pecharsky, V., Bünzli, J.-C. G., Eds.; Elsevier, Amsterdam, 2019; Vol. 56, pp 55−162.

(9) Dexter, D. L. A. Theory of sensitized luminescence in solids. *J. Chem. Phys.* **1953**, 21, 836−850.

(10) Malta, O. L. Mechanisms of non-radiative energy transfer involving lanthanide ions revisited. *J. Non-Cryst. Solids* **2008**, 354, 4770−4776.

(11) Carneiro Neto, A. N.; Moura, R. T.; Malta, O. L. On the mechanisms of non-radiative energy transfer between lanthanide ions: centrosymmetric systems. *J. Lumin.* **2019**, 210, 342−347.

(12) Dexter, D. L.; Schulman, J. H. Theory of concentration quenching in inorganic phosphors. *J. Chem. Phys.* **1954**, *22*, 1063−1070.

(13) Kushida, T. Energy transfer and cooperative optical transitions in rare-earth doped inorganic materials. I. Transition probability calculation. *J. Phys. Soc. Jpn.* **1973**, *34*, 1318−1326.

(14) Blasse, G.; Grabmaier, B. C. *Luminescent materials*; Springer: Berlin, 1994.

(15) Bettinelli, M.; Speghini, A.; Piccinelli, F.; Ueda, J.; Tanabe, S. Energy transfer processes in $Sr_3Tb_{0.90}Eu_{0.10}(PO_4)_3$. *Opt. Mater. (Amsterdam, Neth.)* **2010**, *33*, 119−122.

(16) Carrasco, I.; Bartosiewicz, K.; Nikl, M.; Piccinelli, F.; Bettinelli, M. Energy transfer processes in $Ca_3Tb_{2-x}Eu_xSi_3O_{12}$ (x = 0−2). *Opt. Mater. (Amsterdam, Neth.)* **2015**, *48*, 252−257.

(17) Di, K.; Li, X.; Jing, X.; Yao, S.; Yan, J. Energy transfer and luminescence properties of $KZnF_3$: $Ln^{3+}$ ($Ln^{3+}$ = $Eu^{3+}$, $Tb^{3+}$, $Eu^{3+}$/$Tb^{3+}$, $Eu^{3+}$/$Tb^{3+}$/$Tm^{3+}$) phosphors. *J. Alloys Compd.* **2016**, *661*, 435−440.

(18) Sawada, K.; Nakamura, T. Dynamics of resonance energy transfer process from $Tb^{3+}$ to $Eu^{3+}$ in $Ga_2O_3$ phosphor. *J. Lumin.* **2019**, *215*, 116616.

(19) Bettinelli, M.; Piccinelli, F.; Speghini, A.; Ueda, J.; Tanabe, S. Excited state dynamics and energy transfer rates in $Sr_3Tb_{0.90}Eu_{0.10}(PO_4)_3$. *J. Lumin.* **2012**, *132*, 27−29.

(20) Shyichuk, A.; Câmara, S. S.; Weber, I. T.; Carneiro Neto, A. N.; Nunes, L. A. O.; Lis, S.; Longo, R. L.; Malta, O. L. Energy transfer upconversion dynamics in $YVO_4$:$Yb^{3+}$,$Er^{3+}$. *J. Lumin.* **2016**, *170*, 560−570.

(21) Barbier, J.; Greedan, J. E.; Asaro, T.; McCarthy, G. J. Neutron diffraction study of disorder in eulytite-type $Sr_3La(PO_4)_3$. *Eur. J. Solid State Inorg. Chem.* **1990**, *27*, 855−867.

(22) Judd, B. R. Optical absorption intensities of rare-earth ions. *Phys. Rev.* **1962**, *127*, 750−761.

(23) Ofelt, G. S. Intensities of crystal spectra of rare-earth ions. *J. Chem. Phys.* **1962**, *37*, 511−520.

(24) Jørgensen, C. K.; Judd, B. R. Hypersensitive pseudoquadrupole transitions in lanthanides. *Mol. Phys.* **1964**, *8*, 281−290.

(25) Wybourne, B. G. *Spectroscopic Properties of Rare Earths*; John Wiley & Sons: Hoboken, N.J., 1965.

(26) de Sá, G. F.; Malta, O. L.; de Mello Donegá, C.; Simas, A. M.; Longo, R. L.; Santa-Cruz, P. A.; da Silva, E. F. Spectroscopic properties and design of highly luminescent lanthanide coordination complexes. *Coord. Chem. Rev.* **2000**, *196*, 165−195.

(27) Moura, R. T., Jr; Carneiro Neto, A. N.; Longo, R. L.; Malta, O. L. On the calculation and interpretation of covalency in the intensity parameters of 4f−4f transitions in $Eu^{3+}$ complexes based on the chemical bond overlap polarizability. *J. Lumin.* **2016**, *170*, 420−430.

(28) Malta, O. L. Theoretical crystal-field parameters for the $YOCl$:$Eu^{3+}$ system. A simple overlap model. *Chem. Phys. Lett.* **1982**, *88*, 353−356.

(29) Malta, O. L. A simple overlap model in lanthanide crystal-field theory. *Chem. Phys. Lett.* **1982**, *87*, 27−29.

(30) Bebb, H. B.; Gold, A. Multiphoton ionization of hydrogen and rare-gas atoms. *Phys. Rev.* **1966**, *143*, 1−24.

(31) Malta, O. L.; Gouveia, E. A. Comment on the average energy denominator method in perturbation theory. *Phys. Lett. A* **1983**, *97*, 333−334.

(32) Malta, O. L.; Batista, H. J.; Carlos, L. D. Overlap polarizability of a chemical bond: a scale of covalency and application to lanthanide compounds. *Chem. Phys.* **2002**, *282*, 21−30.

(33) Moura, R. T.; Malta, O. L.; Longo, R. L. The chemical bond overlap plasmon as a tool for quantifying covalency in solid state materials and its applications to spectroscopy. *Int. J. Quantum Chem.* **2011**, *111*, 1626−1638.

(34) Moura, R. T., Jr.; Duarte, G. C. S.; da Silva, T. E.; Malta, O. L.; Longo, R. L. Features of chemical bonds based on the overlap polarizabilities: diatomic and solid-state systems with the frozen-density embedding approach. *Phys. Chem. Chem. Phys.* **2015**, *17*, 7731−7742.

(35) Shyichuk, A.; Moura, R. T.; Neto, A. N. C.; Runowski, M.; Zarad, M. S.; Szczeszak, A.; Lis, S.; Malta, O. L. Effects of dopant addition on lattice and luminescence intensity parameters of Eu(III)-doped lanthanum orthovanadate. *J. Phys. Chem. C* **2016**, *120*, 28497−28508.

(36) Elk Code. http://elk.sourceforge.net/ (accessed 2020-04-10).

(37) Singh, D. J.; Nordström, L. *Planewaves, pseudopotentials and the LAPW method*, 2nd ed.; Springer US, 2006.

(38) Perdew, J. P.; Ruzsinszky, A.; Csonka, G. I.; Vydrov, O. A.; Scuseria, G. E.; Constantin, L. A.; Zhou, X.; Burke, K. Restoring the density-gradient expansion for exchange in solids and surfaces. *Phys. Rev. Lett.* **2008**, *100*, 136406.

(39) te Velde, G.; Bickelhaupt, F. M.; Baerends, E. J.; Fonseca Guerra, C.; van Gisbergen, S. J. A.; Snijders, J. G.; Ziegler, T. Chemistry with ADF. *J. Comput. Chem.* **2001**, *22*, 931−967.

(40) Lee, C.; Yang, W.; Parr, R. G. Development of the Colle-Salvetti correlation-energy formula into a functional of the electron density. *Phys. Rev. B: Condens. Matter Mater. Phys.* **1988**, *37*, 785−789.

(41) Perdew, J. P. Density-functional approximation for the correlation energy of the inhomogeneous electron gas. *Phys. Rev. B: Condens. Matter Mater. Phys.* **1986**, *33*, 8822−8824.

(42) Van Lenthe, E.; Baerends, E. J. Optimized Slater-type basis sets for the elements 1−118. *J. Comput. Chem.* **2003**, *24*, 1142−1156.

(43) Van Lenthe, E.; Snijders, J. G.; Baerends, E. J. The zero-order regular approximation for relativistic effects: the effect of spin-orbit coupling in closed shell molecules. *J. Chem. Phys.* **1996**, *105*, 6505−6516.

(44) Van Lenthe, E.; Baerends, E. J.; Snijders, J. G. Relativistic total energy using regular approximations. *J. Chem. Phys.* **1994**, *101*, 9783−9792.

(45) van Lenthe, E.; Ehlers, A.; Baerends, E.-J. Geometry optimizations in the zero order regular approximation for relativistic effects. *J. Chem. Phys.* **1999**, *110*, 8943−8953.

(46) Tanner, P. A.; Chua, M.; Reid, M. F. Energy transfer by magnetic dipole—magnetic dipole interaction. *Chem. Phys. Lett.* **1993**, *209*, 539−546.

(47) Chua, M.; Tanner, P. A.; Reid, M. F. Energy transfer by electric dipole-magnetic dipole interaction in cubic crystals. *Solid State Commun.* **1994**, *90*, 581−583.

(48) Tanner, P. A.; Chua, M.; Reid, M. F. Energy transfer between lanthanide ions in elpasolite lattices. *J. Alloys Compd.* **1995**, *225*, 20−23.

(49) Chua, M.; Tanner, P. A.; Reid, M. F. Energy transfer between lanthanide ions in elpasolite lattices: electric quadrupole-electric quadrupole interaction. *J. Lumin.* **1994**, *58*, 356−360.

(50) Fano, U.; Racah, G. *Irreducible tensorial sets*, 1st ed., Academic Press Inc., New York, 1959.

(51) Ofelt, G. S. Structure of the $f^6$ configuration with application to rare-earth ions. *J. Chem. Phys.* **1963**, *38*, 2171−2180.

(52) Carnall, W. T.; Crosswhite, H.; Crosswhite, H. M. *Energy level structure and transition probabilities in the spectra of the trivalent lanthanides in $LaF_3$*; ANL Report: Argonne, IL, 1978.

(53) Malta, O. L.; Brito, H. F.; Menezes, J. F. S.; Gonçalves e Silva, F. R.; Alves, S.; Farias, F. S., Jr.; de Andrade, A. V. M. Spectroscopic properties of a new light-converting device Eu-(thenoyltrifluoroacetonate)$_3$ 2(dibenzyl sulfoxide). A theoretical analysis based on structural data obtained from a sparkle model. *J. Lumin.* **1997**, *75*, 255−268.

(54) Berry, M. T.; May, P. S.; Hu, Q. Calculated and observed $Tb^{3+}(^5D_4)$ → $Eu^{3+}$ electronic energy transfer rates in $Na_3[Tb_{0.01}Eu_{0.99}(oxydiacetate)_3]$-$2NaClO_4$-$6H_2O$. *J. Lumin.* **1997**, *71*, 269−283.

(55) Grant, W. J. C. Role of rate equations in the theory of luminescent energy transfer. *Phys. Rev. B* **1971**, *4*, 648−663.

(56) Wright, J. C. In *Radiationless processes in molecules and condensed phases*; Fong, F. K., Ed.; Springer: Berlin, 1976; pp 239−295.

(57) Strek, W. Concentration dependence of the phonon-assisted energy transfer between rare-earth ions. *Phys. Rev. B: Condens. Matter Mater. Phys.* **1984**, *29*, 6957−6962.

(58) Paterlini, V.; Piccinelli, F.; Bettinelli, M. $Tb^{3+} \rightarrow Eu^{3+}$ energy transfer processes in eulytite $A_3Tb(PO_4)_3$ (A = Sr, Ba) and silico-carnotite $Ca_3Tb_2Z_3O_{12}$ (Z = Si, Ge) materials doped with $Eu^{3+}$. *Phys. B* **2019**, *575*, 411685.

(59) Shannon, R. D. Revised Effective ionic radii and systematic studies of interatomic distances in halides and chalcogenides. *Acta Crystallogr., Sect. A: Cryst. Phys., Diffr., Theor. Gen. Crystallogr.* **1976**, *32*, 751−767.

(60) Rodrigues, C. V.; Luz, L. L.; Dutra, J. D. L.; Junior, S. A.; Malta, O. L.; Gatto, C. C.; Streit, H. C.; Freire, R. O.; Wickleder, C.; Rodrigues, M. O. Unusual photoluminescence properties of the 3D mixed-lanthanide−organic frameworks induced by dimeric structures: a theoretical and experimental approach. *Phys. Chem. Chem. Phys.* **2014**, *16*, 14858−14866.

(61) Bettinelli, M.; Flint, C. D. Non-resonant energy transfer between $Tb^{3+}$ and $Eu^{3+}$ in the cubic hexachloroelpasolite crystals $Cs_2NaTb_{1-x}Eu_xCl_6$ (x = 0.01−0.15). *J. Phys.: Condens. Matter* **1990**, *2*, 8417−8426.

(62) Souza, A. S.; Nunes, L. A.; Felinto, M. C. F. C.; Brito, H. F.; Malta, O. L. On the quenching of trivalent terbium luminescence by ligand low lying triplet state energy and the role of the $^7F_5$ level: The $[Tb(tta)_3(H_2O)_2]$ case. *J. Lumin.* **2015**, *167*, 167−171.

(63) Roy, U. N.; Hawrami, R. H.; Cui, Y.; Morgan, S.; Burger, A.; Mandal, K. C.; Noblitt, C. C.; Speakman, S. A.; Rademaker, K.; Payne, S. A. $Tb^{3+}$-doped $KPb_2Br_5$: low-energy phonon mid-infrared laser crystal. *Appl. Phys. Lett.* **2005**, *86*, 151911.

(64) Rademaker, K.; Krupke, W. F.; Page, R. H.; Payne, S. A.; Petermann, K.; Huber, G.; Yelisseyev, A. P.; Isaenko, L. I.; Roy, U. N.; Burger, A.; Mandal, K. C.; Nitsch, K. Optical properties of $Nd^{3+}$- and $Tb^{3+}$-doped $KPb_2Br_5$ and $RbPb_2Br_5$ with low nonradiative decay. *J. Opt. Soc. Am. B* **2004**, *21*, 2117−2129.

(65) Momma, K.; Izumi, F. VESTA 3 for three-dimensional visualization of crystal, volumetric and morphology data. *J. Appl. Crystallogr.* **2011**, *44*, 1272−1276.